Weld inspection by focused adjoint method

Khaled Metwally, Emma Lubeigt, Sandrine T. Rakotonarivo, Jean François Chaix, Francois Baque, Gilles Gobillot, Serge Mensah

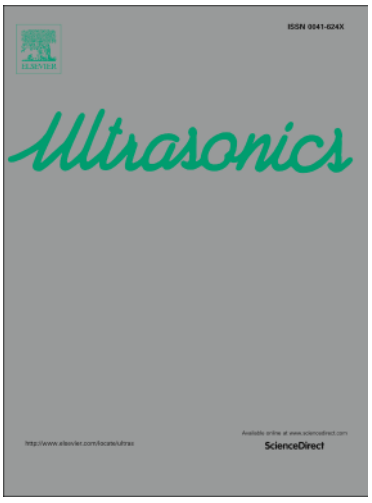

Weld inspection by focused adjoint method

Khaled Metwally, Emma Lubeigt, Sandrine Rakotonarivo, Jean-François Chaix, François Baqué, Gilles Gobillot, Serge Mensah

PII: S0041-624X(17)30270-6
DOI: http://dx.doi.org/10.1016/j.ultras.2017.08.009
Reference: ULTRAS 5603

To appear in: *Ultrasonics*

Received Date: 24 March 2017
Revised Date: 22 August 2017
Accepted Date: 22 August 2017

Please cite this article as: K. Metwally, E. Lubeigt, S. Rakotonarivo, J-F. Chaix, F. Baqué, G. Gobillot, S. Mensah, Weld inspection by focused adjoint method, *Ultrasonics* (2017), doi: http://dx.doi.org/10.1016/j.ultras.2017.08.009

Weld inspection by focused adjoint method

Khaled Metwally[a], Emma Lubeigt[a,b], Sandrine Rakotonarivo[a], Jean-François Chaix[a], François Baqué[b], Gilles Gobillot[b], Serge Mensah[a,*]

[a] *Aix-Marseille Université, CNRS, Centrale Marseille, LMA, Marseille, France*
[b] *CEA, Centre de Cadarache, 13108 Saint-Paul-Lez-Durance Cedex, France*

Abstract

This paper reports a methodology for the non-destructive ultrasonic evaluation of welds, based on probing, residue back-focusing and topological energy calculation using an enhanced (focused) adjoint method. The proposed method combines the advantages of time reversal to compensate for the cumulative distorsions experienced by a wave propagating in a heterogeneous medium, and topological imaging to highlight the defect location. The synergistic effect of this combined approach makes it possible to detect anomalies in the most efficient way. The method paves the way towards a matched-insonification imaging of anomalies in anisotropic media.

Keywords: Topological energy, Adjoint method, Wave focusing, Weld inspection, Finite element modeling

1. Introduction

The non-destructive evaluation (NDE) of austenitic welds using ultrasounds (US) has been gaining a lot of attention in structural health monitoring, which is aimed at damage detection and characterization and structure integrity assessment. Austenitic steels are popular in civil engineering, shipbuilding industries, petrochemical, aviation, and nuclear power plants due to their corrosion resistance, relatively high ductility and high strength compared with typical carbon steels (mild steels or low-alloy steels). The defects that usually encountered in welding include incomplete penetration, incomplete fusion, undercutting, and porosity. More crucially, cracking defects may occur during solidification of the melt pool, which is problematic as they act as stress concentration sites. This could lead to premature failure via fatigue, as well as providing sites open to hydrogen-assisted cracking. However, detecting and locating anomalies is a difficult task since weld microstructures induce strong US-wave deviation and splitting phenomena.

*Corresponding author
Email address: mensah@lma.cnrs-mrs.fr (Serge Mensah)

This microstructure originates from various cooling phenomena. Near the fusion line, atoms from the molten pool are deposited on preexisting lattice sites in the adjacent solid base metal; consequently, the grain structure is dominated by epitaxial growth where the base and the weld metals have the same crystal orientation. Away from that line, however, the grain structure is dominated by a different mechanism named the competitive growth. The latter is characterized by grain directions perpendicular to the fusion boundary, which offers maximum heat extraction (i.e. maximum temperature gradient). This competitive growth mechanism dominates the grain structure of the bulk weld metal and results in a heterogeneous columnar-grain distribution. Another complex phenomenon, solidification cracking, may arise, which involves heat and fluid flows, material chemistry and welding process parameters. Here, as the columnar grains are less permeable, they prevent the liquid metal from reaching strain-localized regions and damage initiation is therefore promoted. Furthermore, the recent use of high-speed, high-energy synchrotron X-ray tomography [1] shows that micro-cavities (average size of 20.10^{-6}m) coalesce into micro-cracks of various sizes and morphologies, which propagate from the core of the weld towards the free surface along the solidifying grain boundaries. Even if the full thermodynamics of the micro-cavity initiation and the fracture growth is not yet fully understood, it appears especially marked when considering a high solidification rate processing of steel such as shielded metal arc welding (SMAW).

Today, already three kinds of elastic SMA-weld models are proposed in the literature, which rely on a single stiffness matrix and grain orientations (based on a common stiffness matrix assumption). Firstly, a piecewise description of the weld, in which the orientations for a set of grains are practically identical, leads to large sub-domains with respect to the wavelength. Secondly, a mapping description has been proposed where the orientation of the grains is defined on a regular grid (2×2 mm^2). Finally, a parametric description is provided in which the grain orientation is defined as a function of coordinates in the weld. The parametric description was proposed in 1985 by Ogilvy as a simplified symmetrical model of the weld structure [2].

Moreover, different numerical methods were implemented to solve elastic wave propagation problems for the non-destructive evaluation of welds, including semi-analytical [3], ray-tracing and finite-element methods. The FEM-based elastodynamic finite integration technique (EFIT) to simulate ultrasound wave propagation was first used by Fellinger *et al.* [4]. The EFIT technique relies upon the discretization of the underlying elastodynamic equations for ultrasonic propagation. A few years later, Halkjaer *et al.* [5] applied this technique to numerically study wave propagation in an austenitic weld. Transmission A-scan signals were used in conjunction with Ogilvy model [2] to estimate the grain orientation. Conjointly, Hannemann used the B-scans to show qualitative agreement in an idealized V-butt weld [6] and Mark *et al.* [7] investigated the elastic crystallographic anisotropy of welds in order to improve ultrasonic inspections.

Chassignole *et al.* [8], [9] developed the 2D finite-element code (ULTSON) to predict ultrasonic wave propagation in isotropic and heterogeneous media.

In this code, the austenitic weld was divided into several homogeneous domains and the columnar-grain directions were determined from X-ray diffraction (XRD) analysis and electron back-scattered diffraction (EBSD) analysis. However, FEM approaches have the disadvantage of extended computation times and physical memory limitations, especially if a large simulation domain is required. This can be overcome by different means. For example, another 2D finite-element code named ATHENA speeds up the computation time by applying a fictitious domain method in which a regular mesh of the calculation domain can be combined with an irregular mesh of the defect area [10]. On the other hand, the numerical model PZFlex takes a finite-element and explicit time-domain approach to solve large complex 1D, 2D, and 3D wave-propagation problems. A probabilistic analysis reported in [11] estimates the uncertainties intervals and sensitivity factors for the ultrasonic simulations of a weld inspection.

Techniques have been developed over the years to improve detection or to speed-up the measurements [12], *e.g.*: synthetic aperture focusing Technique (SAFT), full matrix capture (FMC), sparse matrix capture (SMC), total focusing method (TFM), dynamic depth focusing (DDF), decomposition of time reversal operator (DORT) [13]. Another interesting method called "experimental acoustic signature extraction" was designed for selective focusing within unknown media [14]. It is worth highlighting the FMC technique, which consists in capturing and storing all possible time-domain signals (A-Scans) from every transmitter-receiver pair of elements in the array. After recording, the raw information is available to generate the data for any given beam (aperture, refracted/skew angles and focusing position), through off-line processing. There are, however, several advantages in using the sparse matrix capture (SMC) method instead of FMC. SMC speeds up the acquisition since fewer elements are used and less time is needed to perform the electrical commutations: a smaller quantity of data is recorded and post-processing is much faster.

Most of these methods were initially developed for non-destructive imaging based on the assumption that the medium inspected was either homogeneous or weakly inhomogeneous. Therefore, important efforts are ongoing to make these techniques suitable to anisotropic media such as welds. However, due to the complex ultrasonic ray-paths and wave-defect interactions, only poor-contrast images of the defect or non-constant detection probabilities are obtained.

The aim of this study is to efficiently detect and localize holes or open cracks in a complex and strongly heterogeneous medium, such as a SMA weld, using ultrasounds. The holes in question are located in regions of high and low insonification levels with the purpose of evaluating the ability of the imaging procedure to provide constant detection in the entire region of interest (ROI). The open cracks mimic realistic centerline cracking (less than 100 microns in width) emerging at the bottom side of the welded bar. They are used to assess both the detection power and the shape estimation efficiency (to distinguish cracks from holes). For their detection and characterization, the defects are presented to the end-user in the form of an image obtained after applying the topological energy method [15]. Since this method was derived in free-space homogeneous

media conditions, this study introduces several major improvements which open the door to a high-performance inspection of complex bounded media such as welds.

2. Material and method

2.1. Numerical model for SMA welds

As mentioned in the previous paragraph, the grain structure (size, shape and orientation of the grains) is highly influenced by the temperature gradients and the welding parameters during the solidification process. A random distribution of the grain orientation, size and shape can therefore be characterized and segmentation performed in the transverse plane of the weld.

Consequently, any inspection technique that can be adapted to the inspected weld and provide both satisfactory image contrast and/or localization accuracy should be able to take into account prior information about (the wave propagation through the specification of) the welding process.

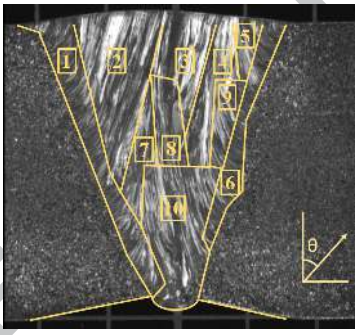

Figure 1: Macrograph of the butt joint described as a piecewise homogeneous domain

For this reason, a finite element method was implemented to conduct 2D numerical simulations of wave propagation (using the COMSOL® structural mechanics module) and defect inspection in a V-butt austenitic weld. Assuming a transverse isotropic material, the SMA welding zone shown in Figure 1 was partitioned into ten homogeneous domains of constant columnar-grain orientations.

The heterogeneous anisotropic domain is therefore described by two sets of parameters:

- Elasticity constants of the medium
- Orientation of the coordinate systems used to express the elasticity constants; this orientation corresponds to the mean grain orientation in the defined sub-domain.

To predict the stiffness maps, it is assumed that:
1/ The material properties of the multi-pass welds are transversely isotropic, with the single principal axis lying in the plane of the cross-section
2/ The grain growth direction corresponds to the local principal direction and that the plane perpendicular to the mean grain-direction is isotropic. It is known that these assumptions are strictly incorrect, because the welding wire moves along the weld line, so that the heat flow and solidification directions are tilted somewhat out of this plane
3/ The material is single phase and only one crystal stiffness tensor can be used for all the material across the weld
4/ The magnitude of the principal stiffness will be constant and its direction will vary with the direction of grain growth. The angle of this principal direction to the plate normal, in the plane of the cross-section, is the only parameter characterized by the simplified stiffness map.

Table 1 lists the elastic coefficients of the 316L stainless steel weld, shown in Fig. 1, determined by ultrasonic measurements. The elastic tensor is expressed using the Voigt notation with plane 13 as the main plane.

Table 1: Elastic coefficients (GPa) of the 316L stainless steel weld determined by ultrasonic measurements. The elastic tensor is expressed using the Voigt notation with plane 13 as the main plane.

C_{11}	C_{12}	C_{13}	C_{22}	C_{44}
243	137	84	212	122 GPa

$$C^{init} = \begin{pmatrix} C_{11} & C_{12} & C_{13} & 0 & 0 & 0 \\ C_{12} & C_{22} & C_{12} & 0 & 0 & 0 \\ C_{13} & C_{12} & C_{11} & 0 & 0 & 0 \\ 0 & 0 & 0 & C_{44} & 0 & 0 \\ 0 & 0 & 0 & 0 & \frac{C_{11}-C_{13}}{2} & 0 \\ 0 & 0 & 0 & 0 & 0 & C_{44} \end{pmatrix}$$

To obtain the coefficients in each area, a rotation matrix was applied to the original coefficients matrix C_{ijkl}.

$$\alpha = \begin{pmatrix} \cos\theta & \sin\theta & 0 \\ -\sin\theta & \cos\theta & 0 \\ 0 & 0 & 1 \end{pmatrix}$$

2.2. Implementation of topological imaging

Topological imaging [16, 17, 18] is a recent NDE method related to time reversal and adjoint methods, which makes it possible to image heterogeneous media. This method was originally developed from optimization approaches used to solve inverse acoustic or elastic problems in the field of geophysics [19, 20, 21] and mechanical structure optimization [22, 23, 24, 25]. The approach consists

Table 2: Orientation θ (°) of the principal axis of the columnar grains and speed of quasi-longitudinal waves of each homogeneous sub-domain of the weld.

Selected zone	1	2	3	4	5	6	7	8	9	10
Orientation angle	29°	15°	13°	9°	-12°	-44°	11°	-7°	-20°	-14°
Sound speed (c_p)	5962	5532	5463	5331	5429	6187	5395	5273	5702	5498

in iteratively constructing a parameter distribution, which provides synthetic data in agreement with the measured data. In that aim, a cost function which quantifies the goodness of fit between predicted and observed data is minimized through the computation of the Fréchet derivative (*i.e.* cost-function gradient). Under the Born approximation, Tarantola and Norton demonstrate that the Fréchet derivative can be computed, both in a fluid medium [20, 26] and in a solid medium [27, 28], by involving the interaction between two numerical wave fields: namely, the forward $\mathbf{u}$ and the adjoint $\tilde{\mathbf{u}}$ fields. It reads (Einstein summation convention):

$$\nabla_{\mathbf{m}}\chi[\mathbf{m}(\mathbf{x})] = \int_0^T \mathbf{\Omega}\tilde{u}_j(\mathbf{x}, T-t)\mathbf{\Omega}u_{0j}(\mathbf{x}, t)dt, \tag{1}$$

where $\mathbf{\Omega}$ is a differential operator which is dependent of the type (density, elasticity constants, grain orientation) of the model parameters $\mathbf{m}(\mathbf{x})$ at each location $\mathbf{x}$. Therefore, in the Born approximation, the total displacement field $\mathbf{u}$ inside the scattering object is replaced by the incident field $\mathbf{u}_0$ present in the surrounding medium, that is assumed to be defect-free, infinite and homogeneous. Considering harmonic waves, this approximation is effective when the contrast is small and as long as the size of the object is not too large relative to the wavelength. The range of validity of the Born approximation is discussed in section 8.10.1 [29]. Noting k the wave number, q the contrast function and $|D|$ the d-dimensional volume of the scatterer ($d = 2$ or 3), two limits are identified:

- in the low-frequency, the long-wavelength limit (i.e. if $k|D|^{\frac{1}{d}} \ll 1$)

$$k^2|D|^{\frac{2}{d}} \max_D |q| \ll 1$$

- in the high-frequency, the short-wavelength limit (i.e. if $k|D|^{\frac{1}{d}} \gg 1$)

$$k|D|^{\frac{1}{d}} \max_D |q| \ll 1$$

Therefore, in the three-dimensional space, under a low-frequency assumption, $k|D|^{\frac{1}{d}} \approx 0.1$, contrast variations up to $q = 10^2$ are tractable. Under a high-frequency assumption, $k|D|^{\frac{1}{d}} \approx 0.1$, the constraint $q < 10^{-2}$ significantly limits the Born approximation applicability.

We looked for a non-iterative method for flaw detection in a bounded domain that does not require a priori knowledge of the flaw shape and location and that is able to localize it using a limited aperture. It is shown in [30] that at high frequencies, the topological sensitivity is asymptotically dominated by the near-boundary terms. When a reduced number of measurements is available, low frequencies are generally preferred. In this case, under the Born approximation assumption, it was demonstrated that the contrast function q can theoretically be recovered up to a characteristic length scale of half the wavelength (low-pass filtering). The full-aperture topological derivative is proportional to [31] $|D|k^4[q * \psi^2](\mathbf{x})$, where $\psi(\mathbf{x}) = 4\pi \sin_c(k|\mathbf{x}|)$ is analytic everywhere and $*$ is the convolution product. Consequently, it is not the contrast object q which can be recovered but only its filtered version $q * \psi^2$. Thus, unless specified, the object contrast considered (in the following) is the filtered one, which is therefore analytic.

In the present study, accurate defect (holes or open cracks) imaging is achieved using a cost efficient approach that involves computation of the single time-domain (broad-band waves) topological derivative (cf Eq. 1). In practice, the evaluation of the Fréchet derivative first consists in insonifying and measuring the broad-band reflectivity responses of the reference and the inspected media using a linear transducer array. It is well known, when operating with reflection measurements, that the parameter resulting in the higher resolution is the longitudinal wave impedance. Assuming (transverse) isotropy of each of the sub-regions, the wave impedance is defined as:

$$Z_p(\mathbf{x}) = \rho(\mathbf{x}) c_p(\mathbf{x}) = \sqrt{\rho(\mathbf{x})(\lambda(\mathbf{x}) + 2\mu(\mathbf{x}))}, \tag{2}$$

where λ and μ are Lamé parameters, c_p is the speed of the pressure waves and ρ is the density. Thus, under the assumption of a constant density ρ, the Fréchet derivative with respect to a longitudinal wave impedance variation is linearly related to the Fréchet derivative with respect to the first Lamé parameter:

$$\nabla_{Z_p} \chi[\mathbf{m}(\mathbf{x})] = 2c_p(\mathbf{x}) \nabla_\lambda \chi[\mathbf{m}(\mathbf{x})]. \tag{3}$$

The operator describing a variation in the first Lamé parameters is the divergence operator, $\mathbf{\Omega}_\lambda = \boldsymbol{\nabla}$. [21].

Furthermore, in case of fluctuations in the grain orientations less than 45° (see Table 2), $\delta c_p(\mathbf{x})/c_p(\mathbf{x}) < 12\%$ (with a standard deviation less than 5.5%). Thus, we assume as a first approximation that $c_p(\mathbf{x}) \approx cste$. A robust representation of the Fréchet derivative is given by the topological energy [17] defined as:

$$TE(\mathbf{x}) = \int_0^T |\nabla.\tilde{\mathbf{u}}(\mathbf{x}, T-t)| \, |\nabla.\mathbf{u}_0(\mathbf{x}, t)| \, dt. \tag{4}$$

This topological energy method (TEM) has been investigated with acoustic and elastic waves [32, 17, 33], with dispersive waves [18] and with anisotropic waves [34]. The method successfully highlights defects considered as relevant distinctions when compared with the reference model. However, difficulties to

apply this process in a bounded medium arise because multiple reflections of the forward and adjoint fields occur and may coexist at different times and locations during the whole duration of the acquisition, therefore generating spurious artifacts.

This issue has been addressed by the authors in a recent study [35] where two modified topological energies were derived; each of them selects the relevant information according to the defect (hole or slit) to analyze. By modifying the boundary conditions in the numerical model, it was shown that unwanted artifacts due to reflections on the edges can be totally removed. This greatly improves hole detection and localization performance in a stainless steel (homogeneous) block. To suppress these reflections, Dirichlet or Neumann boundaries conditions were in turns applied in order to build a reflection-free adjoint field $\tilde{\mathbf{u}}_\Sigma$, namely the *scattering adjoint field* (respectively, a free-space direct field $\mathbf{u}_\Sigma$), as the sum:

$$\tilde{\mathbf{u}}_\Sigma(\mathbf{x},t) = \frac{\tilde{\mathbf{u}}_\mathcal{D}(\mathbf{x},t) + \tilde{\mathbf{u}}_\mathcal{N}(\mathbf{x},t)}{2}. \tag{5}$$

where the subscripts $\mathcal{D}$ or $\mathcal{N}$ indicate the corresponding (Neumann or Dirichlet) boundaries conditions applied when computing the adjoint or incident fields. Therefore, a *scattering topological image* is derived:

$$TE_{\Sigma\Sigma}(\mathbf{x}) = \int_0^T |\nabla.\tilde{\mathbf{u}}_\Sigma(\mathbf{x},T-t)|\,|\nabla.\mathbf{u}_\Sigma(\mathbf{x},t)|\,dt. \tag{6}$$

The scattering topological imaging was successfully tested (on numerical and experimental data) in order to detect and to size several manufactured slits.

Nevertheless, when applied to a complex medium such as a weld, the image quality observed degrades rapidly as the inspection depth increases. At a given middle depth, this is manifested by hole detection and rendering performance that is highly dependent on the flaw location in the weld. At deeper locus, the defect cannot even be detected. The reason for such degradation is analyzed hereafter and a solution to address this issue is proposed.

2.3. Origin of the topological image contrast degradation

Let us first analyze the origin of the poor contrast observed (for instance on Fig. 6) when performing the topological image of a heterogeneous medium. A point source at location $\mathbf{x}_s$ transmits the same spherical wave in the reference and in the perturbed media. After propagation, pairs of signals are measured on the respective N receiving points $\{\mathbf{x}_r, r = 1, ..., N\}$ and the residue is calculated for each receiver. The defect is assumed to be a punctual perturbation with an isotropic form function V_d at location $\mathbf{x}_d$. Thus, it is represented as $V_d\delta(\mathbf{x}-\mathbf{x}_d)$ with $V_d = 1$ in the following. The residue is composed of waves that undergo single and multiple scattering events, which have interacted with the perturbation.

When the medium is assumed stationary, the residue can be written as follows:

$$\Delta u(\mathbf{x}_r, t) = g(\mathbf{x}_r, t|\mathbf{x}_d) * \left[\sum_{m=0}^{+\infty} g(\mathbf{x}_d, t|\mathbf{x}_d)^{*m}\right] * g(\mathbf{x}_d, t|\mathbf{x}_s) * \phi(\mathbf{x}_s, t), \tag{7}$$

where the sign $*$ stands for the convolution product and $f(t)^{*m}$ refers to f convoluted m times. Term $\phi(\mathbf{x}_s, t_s)$ represents the source and $g(\mathbf{x}, t|\mathbf{x}_s, t_s)$ is the full Green function of the bounded medium. All multiple interactions with the medium boundaries and medium heterogeneities are included in this Green function. This describes the mth order interaction of the scattered wave with the defect.

Adjoint field. The adjoint field represents the propagation of the time-reversed residue from the receivers:

$$\tilde{u}(\mathbf{x}, t) = \sum_{r=1}^{N} \int_0^T g(\mathbf{x}, t|\mathbf{x}_r, t_r) \Delta u(\mathbf{x}_r, T - t_r)\, dt_r. \tag{8}$$

By substituting 7 into 8:

$$\tilde{u}(\mathbf{x}, t) = \sum_{r=1}^{N} \int_0^T g(\mathbf{x}, t|\mathbf{x}_r, t_r) g(\mathbf{x}_r, T - t_r|\mathbf{x}_d)\, dt_r * \left[\sum_{m=0}^{+\infty} g(\mathbf{x}_d, t|\mathbf{x}_d)^{*m}\right] * g(\mathbf{x}_d, t|\mathbf{x}_s) * \phi(\mathbf{x}_s, t). \tag{9}$$

In the expression above, the first-order term of the RHS ($m = 0$) equals to:

$$\sum_{r=1}^{N} \int_0^T g(\mathbf{x}, t|\mathbf{x}_r, t_r) g(\mathbf{x}_r, T - t_r|\mathbf{x}_d)\, dt_r * g(\mathbf{x}_d, t|\mathbf{x}_s) * \phi(\mathbf{x}_s, t), \tag{10}$$

and corresponds to the scattered and reflected waves in the bounded medium D (for instance the infinite plate), which are back-propagated from the receivers and observed at a point $\mathbf{x}$. In the case $m = 0$, there are no multiple interactions of the scattered field with the perturbation. If a broadband source is considered, $\phi(\mathbf{x}_s, t) = \delta(\mathbf{x} - \mathbf{x}_s)\delta(t)$, Eq. 10 is the expression of a cross-correlation that reaches a maximum at the perturbation's location $\mathbf{x} = \mathbf{x}_d$ and at time $t = T - \frac{|\mathbf{x}_d - \mathbf{x}_s|}{c}$. The higher-order terms of expression 7 are maximized at the same location but for different times. The topological energy (Eq. 4) is used to obtain an estimate of the defect location.

In order to have a better understanding of what happens in case of heterogeneous media, let us reformulate the impulse response of the medium that

describes the complete Green function between the punctual source $\mathbf{x}_s$ and the punctual-defect location $\mathbf{x}_d$ under the form:

$$g(\mathbf{x}_d, t|\mathbf{x}_s) = \sum_{j=1}^{Q(T)} g_{dj}\delta(t - \Theta_j), \tag{11}$$

where g_{dj} stands for the wave amplitude and phase shift (resulting from the various interactions with the heterogeneities, the wave attenuation, etc) evaluated at $\mathbf{x}_d$ at the time Θ_j. Considering multiple ray-paths, the travel-times Θ_j between the source and the defect location are ordered according to the values of the subscript j. $Q(T)$ is the total number of replica impinging on the defect during the acquisition duration T.

Substituting this relation in Eq. 10, the adjoint field can be resumed as follows:

$$\begin{aligned} v(\mathbf{x}, t) &= \sum_{r=1}^{N}\sum_{j=1}^{Q(T)} g_{dj}\Lambda_{r,j}(\mathbf{x}, t - T + \Theta_j) * \phi(\mathbf{x}_s, t) \\ &= \underset{\mathrm{N,T}}{\Lambda}(\mathbf{x}, t) * \phi(\mathbf{x}_s, t), \end{aligned} \tag{12}$$

where

$$\Lambda_{r,j}(\mathbf{x}, t) = \int_{-\Theta_j}^{T-\Theta_j} g(\mathbf{x}_r, \tau_r|\mathbf{x}, 0)g(\mathbf{x}_r, \tau_r - t|\mathbf{x}_d, 0)\, d\tau_r \tag{13}$$

is the cross-correlation function between the Green functions $g(\mathbf{x}_r, t|\mathbf{x}, 0)$ and $g(\mathbf{x}_r, t|\mathbf{x}_d, 0)$. The following expression

$$\underset{\mathrm{N,T}}{\Lambda}(\mathbf{x}, t) = \sum_{r=1}^{N}\sum_{j=1}^{Q(T)} g_{dj}\Lambda_{r,j}(\mathbf{x}, t - T + \Theta_j) \tag{14}$$

appears as the coherent summation of all these cross-correlation functions, weighted by the complex (gain and phase shift) reflection coefficients g_{dj} of the ray-path associated with each heterogeneity. Therefore, when operating with a finite transducer bandwidth, an interference pattern is created that presents constructive or destructive patterns depending on the position $\mathbf{x}$. In other words, the level of energy that is back-focused on the defect is highly dependent on the position of the pixel (or voxel) considered. On the one hand, if the spatial density of the scatterers is high and/or the correlation length is short with respect to the wavelength, then speckle noise can develop. On the other hand, if the medium is partitioned into piecewise homogeneous sub-regions, then the medium presents waveguide characteristics whose deleterious effects (ray splitting and attenuation) increase with the inspection depth. Ideally, $Q(T)$ would reduce to one since in this case only the wave scattered by the defect propagates and no destructive interferences exist. This is precisely what will be achieved in the proposed methodology.

The natural way to lower the number of ray paths $Q(T)$ crossing the defect would be to limit the distance between the adjoint source (in practice, constituted by the probe transducers) and the defect to a few wavelengths. While this seems, at first glance, completely unrealistic in practice, the time-reversal principle in conjunction with the reciprocity theorem offers an elegant way to create such a physical source of arbitrary shape and waveform inside the medium.

In-depth source synthesis. In order to achieve this, the required source is virtually activated (numerical simulation) at the locus of interest inside the medium; for instance, the source may be placed in a sensitive region highly suspected to host flaws induced by the weld solidification process. The burst wave thus created at time $t = 0$ virtually propagates inside the numerical model of the heterogeneous medium and arrived at the receivers' locations where it is acquired and stored for a duration Υ. Applying the time-reversal principle on each elementary signals $s_{v,r}(t)$ (in practice, a pressure wave $s_{v,r}(\Upsilon - t)$ is transmitted by each piezo-element of the probe), the back-focusing process enables one to synthesize a real (physical, although slightly degraded) copy of the initial virtual wave. The physical-wave avatar presents most of the characteristics required for the detection, localization and sizing of a suspected defect. For instance, it can be expected that a plane wave of limited wavefront support and of constant amplitude (along that support) was generated so the hole detection probability would be constant inside the medium. Figure 2 shows the flow chart of the *focused adjoint method* (FAM) implemented, which comprises two main modules. On the left side of the chart, the in-depth source synthesis module is described. Therefore, once the virtual source is activated, all the elements of the transducer receive the waves after propagation (numerical model) in the weld. As explained previously, the latter has been simplified to ten homogeneous sub-regions with different average grain-orientation angles. These mean orientations naturally affect the local c_{ijkl} matrix and consequently the energy paths followed, i.e. the longitudinal and shear waves developments in each of these regions. The received multi-element signals contain considerable information about the propagation (including pressure/shear modes conversions and pathway) and form the sinogram. By time reversing this sinogram, the new physical source is generated, which can be placed anywhere in the domain, and especially in the vicinity of the expected flaw. Since all the perturbations that affect the propagation of the virtual waves are *i)* taken into account and *ii)* naturally compensated during back-focusing, all the desired source properties can be retrieved with a rather good approximation.

The information related to the defect can then be extracted by solving the forward problem of wave propagation in the weld model according to the (standard (Eq. 4) or scattering (Eq. 6)) *topological imaging* procedure [35] described on the right side of the chart. The reference and inspected media are insonified by a linear transducer array. Each point source at location $\mathbf{x}_s$ transmits a spherical wave to both media. Signals are measured on N receiving points $\{\mathbf{x}_r, r = 1, ..., N\}$ after wave propagation into the media. The residue at the

receivers $\Delta u(\mathbf{x}_r, t)$ is then computed as:

$$\Delta u(\mathbf{x}_r, t) = u_0(\mathbf{x}_r, t) - u_{obs}(\mathbf{x}_r, t), \tag{15}$$

where u_0 and u_{obs} are the divergence of the displacements measured in the unperturbed and inspected media respectively. The time-reversed residue is an ultrasonic signature of the perturbation at the receiver locations, which back-focuses on the defect. The computation of either standard or scattering topological energies provides images of the defect signature.

In the detection framework, in order to evaluate the benefit of the in-depth source synthesis within heterogeneous media, simulations were carried out using a reduced-aperture limited to the upper width of the butt joint which encompasses 40 of the 64 transducer elements (the inter-element pitch equals to 0.8 mm). Firstly, the forward energy flow was calculated using an impulsive plane wave with a central frequency of $f_{central}$ = 2.1 MHz, (bandwidth of 1.6 MHz at -6 dB, f_{max}= 2.9 MHz). The signal, sampled at 39,17 MHz, is analytically computed as the product of a Gaussian envelop (with a FWHM equals to $1/[2.f_{central}]$) and the sinusoidal signal, $\sin(2\pi.f_{central}.t)$.
The meshing of the domain is correlated to the slowest wave speed (the shear wave speed, $c_s = 3137$ m/s); the maximum mesh element size of 0.18 mm is less than $\lambda/6$, where $\lambda = c_s/f_{max}$.
Two 316L stainless steel plates of 40 mm thick were assembled by the weld joint. The density of the base metal was $\rho = 7942$ kg.m^{-3}, Poisson's ratio and the Young's modulus were $\nu = 0.28$ and $E = 200.8$ GPa, respectively. The experimental welded bar was inspected in air by contact measurements and all defects were filled with air (free interfaces).

Nota: In the figures presented hereafter, the reduced aperture used for the plane-wave transmission is depicted in red, the aperture used to acquire and back-focus the residue is plotted in green, the aperture used to synthesize the in-depth source is represented in mauve color.

3. Results and discussion

Figure 3a shows the forward-energy flow (integrated over time) transmitted from a reduced-aperture placed on the top-face of the weld referenced D717C. While a reduced-aperture is employed, the grain orientation distribution implies that an important part of the deposited energy is released (*i.e.* lost) from the weld. Furthermore, the energy distribution inside the weld is irregular. By applying the source synthesis (cf. Fig. 3b), the energy flow path was modified; *i)* the energy deposit at the focusing line was greatly equalized, *ii)* the energy leak out of the weld spot was eliminated. This made it possible to homogenize the detection probability of anomalies located in the vicinity of the source.

Two defects were placed at different locations with respect to the energy path, inside weld D717C, associated with a plane-wave illumination by the

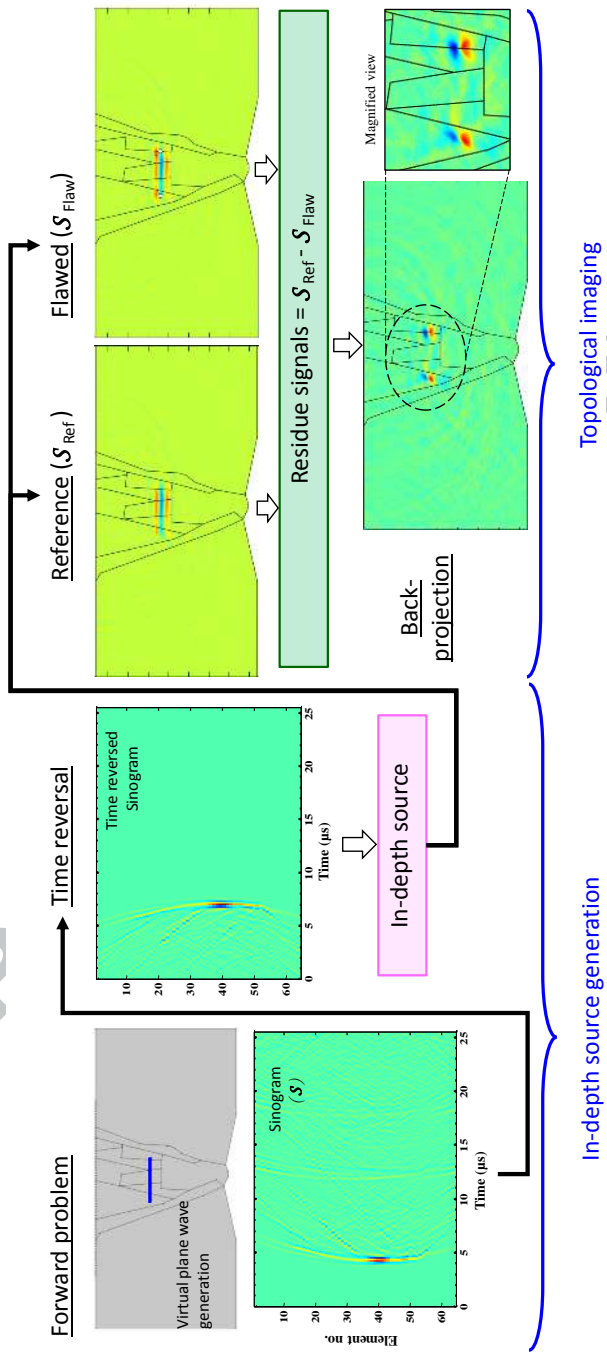

Figure 2: Flow chart of the focused adjoint method (FAM)

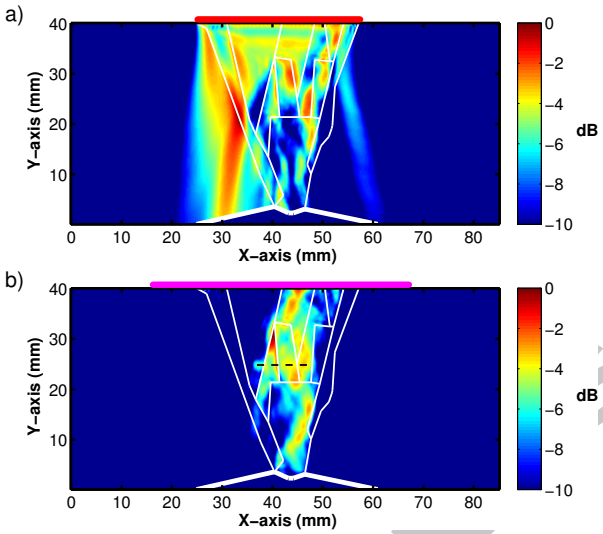

Figure 3: Comparison between energy flow path in both: a) plane-wave excitation (reduced aperture colored in red), b) time-reversed selective focusing excitation (full aperture marked in mauve color)

probe. The hole was either placed within the energy flow path or far away from it. The same experiment was conducted using the in-depth plane wave synthesis and the topological images were compared. In Fig. 4a, the hole placed in the high-energy zone (right spot in the figure) was clearly highlighted relative to the second defect placed in the "dark zone" (left spot in the figure), which was almost 6dB less powerful although the two holes were identical. However, by applying the FAM method, the topological image in Fig. 4c reveals both defects in the weld with intensity variations less than to 2dB. The corresponding zoomed images are given on Fig. 4b and Fig. 4d.

Figure 6 shows the energy distribution associated with a limited plane-wave support generated at a depth of 24mm in the D717C-weld. Fig. 7 shows that by synthesizing an in-depth source, a 15×0.10 mm^2 crack is clearly detected on the topological image, which is not the case (cf. Fig. 5) when the plane wave is transmitted by the multi-element transducer from the top surface. In addition, an extra experiment was carried out considering a simple hole of an equivalent diameter ($\phi = 0.1$ mm) placed at the tip crack location and whose topological image is given in Fig. 8. Comparing Fig. 7 and Fig. 8, the signatures of both defects are clearly distinguishable; an area of high intensity can be seen at the notch-foot region, and an inclined trail is visible along the length of the crack. Once again, the slight drift of this trail is a consequence of the grain orientation in that sub-region.

It is worth noting that the proposed method is conditioned upon the assumption of reciprocity of the wave propagation. This fails in the case of certain configurations presented in [36] for nonreciprocal acoustics. In this case,

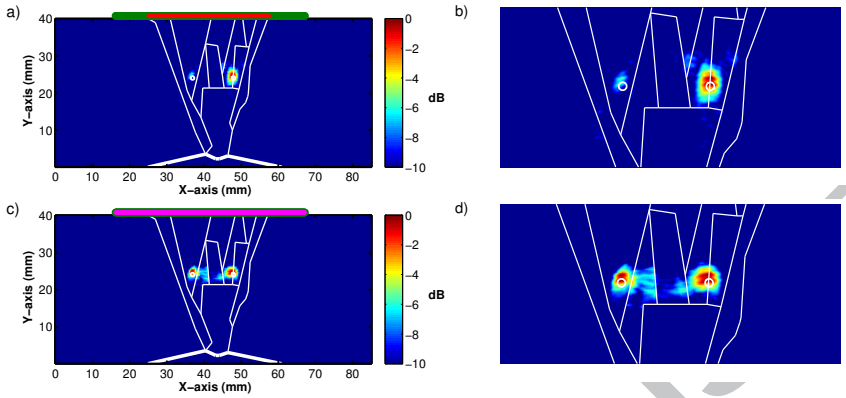

Figure 4: Comparison between topological images: a) plane-wave excitation (using the reduced aperture colored in red), b) Magnified view of the zone of interest c)time-reversal focused excitation using the full (mauve) aperture, d) Magnified view of c). The residue of the topological methods is acquired and back-focused using the full (green) aperture.

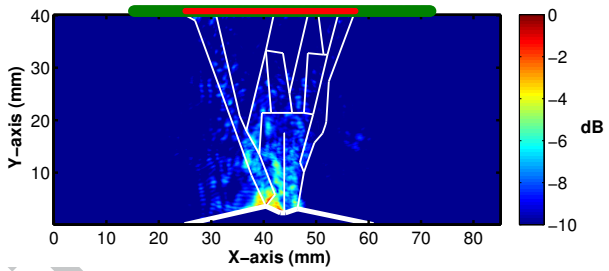

Figure 5: Topological energy of 100μm crack using the scattering adjoint method

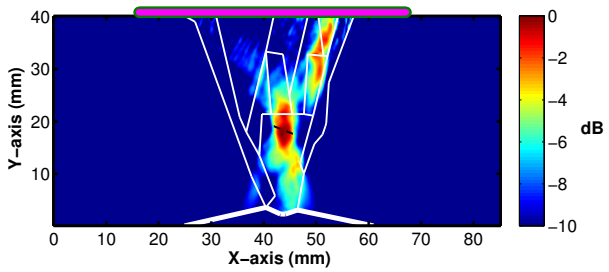

Figure 6: Energy flow path associated to a 5-mm linear source synthesis transmitting a 2-MHz plane wave at a 24-mm depth

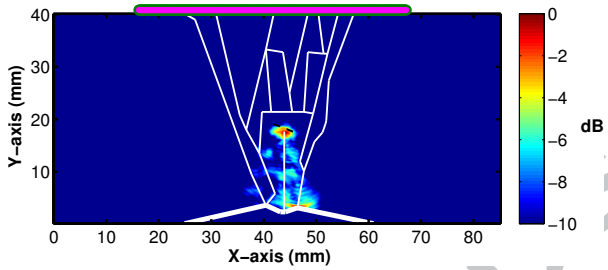

Figure 7: Topological energy of 100μm crack using the focused adjoint method (same conditions as Fig. 6)

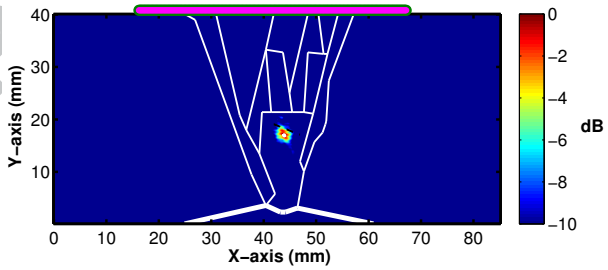

Figure 8: Hole of a 100-μm diameter located at the tip of the crack in Fig. 7 using the focused adjoint method (same conditions as Fig. 6)

the energy flow differs between forward and backward paths. As far as the D717C-weld is concerned, it can be seen in Fig. 3b that energy accumulation occurs in sub-region number 7; after impingement on the sub-region boundaries, an incident wave is reflected and bounces up and down on the top-corner sides that behave like a sound trap. Here, the reciprocity theorem does not apply and artifacts can be produced.

4. Conclusions and perspectives

It has been analytically demonstrated in this paper that within heterogeneous media such as welds, the adjoint field used to calculate the Fréchet derivative of the misfit function is, at a given pixel, a coherent summation of all the replica (due to boundaries or heterogeneities) of the back-propagated residual wave (adjoint source). Depending on the elastic properties of the heterogeneous medium considered, various interference schemes can develop. Either the correlation length of the medium is small relative to the wavelength and speckle noise blurs the topological image, or the complex medium (such as a weld) is partitioned into large sub-regions which induce splitting and deviations in the ultrasonic beam (waveguide-like behavior). In this case, the topological image is subjected to an uneven energy distribution, or in other words, "shadow" zones exist where the flaw detection probability is low. In order to cancel at the target zone, the cumulative alterations of the wave propagating long distances from the receivers to the defect, the synthesis of ultrasonic sources embedded in the medium has been considered. Such sources can be created thanks to the time-reversal technique in conjunction with the reciprocity principle. In practice, this principle may be violated locally, as in the case, for instance, of geometrical sound-traps. However, it is expected that the desired synthetic source be generally nicely approximated and generated within the region of interest. This approach makes it possible to produce arbitrary waves anywhere in the weld, especially in the vicinity of an expected flaw (*e.g.* to address an early warning sign). In this perspective, the design and use of waveforms suitable to a given defect can significantly improve the sensitivity and specificity of the topological imaging system. Furthermore, the latter can be supported by a relevant database enriched along the way by operating experience (OPEX).

Acknowledgments

This work has been carried out within the framework of CEA Project for future Generation 4 nuclear plants. The authors would like to thank Gilles Corneloup for his valuable discussion on weld defects and Bertrand Chassignole for the macrographic grains orientation measurements of the D717C weld in austenitic stainless steel.

[1] L. Aucott, D. Huang, H. B. Dong, S. W. Wen, J. A. Marsden, A. Rack, A. C. F. Cocks, Initiation and growth kinetics of solidification cracking during welding of steel, Scientific Reports 7 (2017) 40255 EP –.

[2] J. Ogilvy, Computerized ultrasonic ray tracing in austenitic steel, NDT international 18 (2) (1985) 67–77.

[3] P. Calmon, S. Mahaut, S. Chatillon, R. Raillon, Civa: an expertise platform for simulation and processing ndt data, Ultrasonics 44 (2006) e975–e979.

[4] P. Fellinger, R. Marklein, K. Langenberg, S. Klaholz, Numerical modeling of elastic wave propagation and scattering with efit—elastodynamic finite integration technique, Wave motion 21 (1) (1995) 47–66.

[5] S. Halkjær, M. P. Sørensen, W. D. Kristensen, The propagation of ultrasound in an austenitic weld, Ultrasonics 38 (1) (2000) 256–261.

[6] R. Hannemann, R. Marklein, K. Langenberg, C. Schurig, B. Köhler, F. Walte, S. Kallsen, C. Nessa, D. O. Thompson, D. E. Chimenti, et al., Ultrasonic wave propagation in real-life austenitic v-butt welds: Numerical modeling and validation, in: AIP Conference Proceedings, Vol. 509, AIP, 2000, pp. 145–152.

[7] A. Mark, Z. Fan, F. Azough, M. Lowe, P. Withers, Investigation of the elastic/crystallographic anisotropy of welds for improved ultrasonic inspections, Materials Characterization 98 (2014) 47–53.

[8] B. Chassignole, D. Villard, M. Dubuget, J.-C. Baboux, R. E. Guerjouma, Characterization of austenitic stainless steel welds for ultrasonic NDT, Review of progress in qualitative non destructive evaluation : volume 19 509 (2000) 1325–1332.

[9] J. Moysan, A. Apfel, G. Corneloup, B. Chassignole, Modelling the grain orientation of austenitic stainless steel multipass welds to improve ultrasonic assessment of structural integrity, International Journal of Pressure Vessels and Piping 80 (2003) 77–85.

[10] A. Apfel, J. Moysan, G. Corneloup, T. Fouquet, B. Chassignole, Coupling an ultrasonic propagation code with a model of the heterogeneity of multipass welds to simulate ultrasonic testing, Ultrasonics 43 (6) (2005) 447–456.

[11] F. Rupin, G. Blatman, S. Lacaze, T. Fouquet, B. Chassignole, Probabilistic approaches to compute uncertainty intervals and sensitivity factors of ultrasonic simulations of a weld inspection, Ultrasonics 54 (4) (2014) 1037–1046.

[12] L. W. Schmerr Jr, Phased array system functions, in: Fundamentals of Ultrasonic Phased Arrays, Springer, 2015, pp. 195–209.

[13] L. J. Cunningham, A. J. Mulholland, K. M. Tant, A. Gachagan, G. Harvey, C. Bird, The detection of flaws in austenitic welds using the decomposition of the time-reversal operator, in: Proc. R. Soc. A, Vol. 472, The Royal Society, 2016, pp. 1–17.

[14] S. Rodriguez, X. Jacob, V. Gibiat, Selective focusing through target identification and experimental acoustic signature extraction: Numerical experiments, Ultrasonics 68 (2016) 8–16.

[15] S. Rodriguez, P. Sahuguet, V. Gibiat, X. Jacob, Fast topological imaging, Ultrasonics 52 (8) (2012) 1010–1018.

[16] N. Dominguez, V. Gibiat, Y. Esquerre, Time domain topological gradient and time reversal analogy: an inverse method for ultrasonic target detection, Wave Motion 42 (2005) 31–52.

[17] N. Dominguez, V. Gibiat, Non-destructive imaging using the time domain topological energy method, Ultrasonics 50 (2010) 367–372.

[18] S. Rodriguez, M. Deschamps, M. Castaings, E. Ducasse, Guided wave topological imaging of isotropic plates, Ultrasonics 54 (2014) 1880–1890.

[19] A. Tarantola, Linearized inversion of seismic reflection data, Geophysical Prospecting 32 (1984) 998–1015.

[20] A. Tarantola, Inversion of seismic reflection data in the acoustic approximation, Geophysics 49 (1984) 1259–1266.

[21] P. Mora, Nonlinear two-dimensional elastic inversion of multi-offset seismic data, Geophysics 52 (1987) 1211–1228.

[22] S. Garreau, P. Guillaume, M. Masmoudi, The topological asymptotic for PDE systems: the elasticity case, SIAM journal on control and optimization 39 (2001) 1756–1778.

[23] M. Bonnet, Topological sensitivity for 3D elastodynamic and acoustic inverse scattering in the time domain, Computer methods in applied mathematics and engineering 195 (2006) 5239–5254.

[24] M. Bonnet, Topological sensitivity of energy cost functional for wave-based defect identification, Comptes Rendus Mécanique 338 (2010) 377–389.

[25] V. Kobolev, Topological derivatives for fundamental frequencies of elastic bodies, Engineering Optimization 48 (2016) 53–72.

[26] S. J. Norton, Iterative inverse scattering algorithms: Methods of computing Fréchet derivatives, J. Acoust. Soc. Am. 106 (1999) 2653–2660.

[27] A. Tarantola, Theoretical background for the inversion of seismic waveforms, including elasticity and attenuation, Pure and applied geophysics 128 (1988) 365–399.

[28] J. Tromp, C. Tape, Q. Liu, Seismic tomography, adjoint methods, time reversal and banana-doughnut kernels, Geophysical Journal International 160 (2005) 195–216.

[29] W. C. Chew, Waves and fields in inhomogeneous media, IEEE press New York, 1995.

[30] B. B. Guzina, F. Pourahmadian, Why the high-frequency inverse scattering by topological sensitivity may work, in: Proc. R. Soc. A, Vol. 471, 2015, p. 20150187.

[31] C. Bellis, M. Bonnet, F. Cakoni, Acoustic inverse scattering using topological derivative of far-field measurements-based L2 cost functionals, Inverse Problems 29 (2013) 075012.

[32] V. Gibiat, P. Sahuguet, Wave guide imaging through time domain topological energy, Ultrasonics 50 (2) (2010) 172–179.

[33] R. Tokmashev, A. Tixier, B. B. Guzina, Experimental validation of the topological sensitivity approach to elastic-wave imaging, Inverse Problems 29 (2013) 125005.

[34] S. Rodriguez, M. Deschamps, M. Castaings, E. Ducasse, Topological imaging of defects in anisotropic plates, in: EWSHM-7th European Workshop on Structural Health Monitoring, 2014, pp. 1155–1162.

[35] E. Lubeigt, S. Mensah, S. Rakotonarivo, J.-F. Chaix, F. Baque, G. Gobillot, Topological imaging in bounded elastic, Ultrasonics 76 (2017) 145–153.

[36] R. Fleury, D. Sounas, M. Haberman, A. Alù, Nonreciprocal acoustics, Acoustics Today 11 (3) (2015) 14–21.

- Efficient detection and characterization of holes or open cracks in shielded metal arc weld using an elastic-wave propagation model is proposed.
- By developing virtual in-depth source synthesis, noise blurring reduction in topological energy images is analytically and numerically demonstrated.
- Improved detection probability as well as an enhanced topological image quality are obtained.